Materials Science & Engineering C 108 (2020) 110494

Contents lists available at ScienceDirect

Materials Science & Engineering C

journal homepage: www.elsevier.com/locate/msec

PVP-stabilized tungsten oxide nanoparticles: pH sensitive anti-cancer platform with high cytotoxicity

Anton L. Popov[a], Bingyuan Han[b], Artem M. Ermakov[a], Irina V. Savintseva[a], Olga N. Ermakova[a], Nelly R. Popova[a], Alexander B. Shcherbakov[c], Taisiya O. Shekunova[d,e], Olga S. Ivanova[e], Daniil A. Kozlov[d,e], Alexander E. Baranchikov[e], Vladimir K. Ivanov[e,f,*]

[a] Institute of Theoretical and Experimental Biophysics, Russian Academy of Sciences, Pushchino, Moscow region 142290, Russia
[b] Jiangsu University of Technology, Zhenjiang 212013, China
[c] Zabolotny Institute of Microbiology and Virology, National Academy of Sciences of Ukraine, Kyiv D0368, Ukraine
[d] Lomonosov Moscow State University, Moscow 119991, Russia
[e] Kurnakov Institute of General and Inorganic Chemistry, Russian Academy of Sciences, Moscow 119991, Russia
[f] National Research Tomsk State University, Tomsk 634050, Russia

A B S T R A C T

Photochromic tungsten oxide (WO_3) nanoparticles stabilized by polyvinylpyrrolidone (PVP) were synthesized to evaluate their potential for biomedical applications. PVP-stabilized tungsten oxide nanoparticles demonstrated a highly selective cytotoxic effect on normal and cancer cells *in vitro*. WO_3 nanoparticles were found to induce substantial cell death in osteosarcoma cells (MNNG/HOS cell line) with a half-maximal inhibitory concentration (IC50) of 5 mg/mL, while producing no, or only minor, toxicity in healthy human mesenchymal stem cells (hMSc). WO_3 nanoparticles induced intracellular oxidative stress, which led to apoptosis type cell death. The selective anti-cancer effects of WO_3 nanoparticles are due to the pH sensitivity of tungsten oxide and its capability of reactive oxygen species (ROS) generation, which is expressed in the modulation of genes involved in reactive oxygen species metabolism, mitochondrial dysfunction, and apoptosis.

1. Introduction

In recent years, many efforts have been made to design and investigate new nanoscale engineered materials for biomedical use [1–7]. The very special physical and chemical properties of nanomaterials allow for their wide application in the diagnostics and treatment of socially significant diseases. WO_3 NP_S have been employed as antibacterial coatings, contrast agents for X-ray computed tomography and biosensors [8–10]. Due to their local plasmon resonance, WO_3 NP_S can be used in photothermal cancer therapy [11,12]. Shaker et al. synthesized dopamine-conjugated hyaluronic acid WO_3 nanoparticles (WO_3-HA), demonstrating efficient photothermal conversion with time-dependent target accumulation in tumors [13]. Bin Zheng et al. used WO_3-loaded macrophages to improve tumor killing *in vivo* [14]. Liu et al. used PEGylated WO_3 nanoparticles as photothermal agents upon NIR laser excitation (980 nm, 0.5 W cm^{-2}) and as an efficient CT imaging contrast agent on a tumor-bearing mouse model [15]. Clark et al. showed that WO_3/Pt nanoparticles, prepared using photodeposition from chloroplatinic acid, promoted light-induced lipid peroxidation and lysosomal instability within 4T1 breast cancer cells. Upon irradiation, WO_3/Pt nanoparticles generated hydroxyl radicals and activated the lipid peroxidation pathway [16]. Other researchers have varied the doping level and the habitus of WO_3 nanoparticles to improve the efficiency of photodynamic therapy. For example, Zhou et al. suggested a facile method to prepare PEGylated tungsten oxide nanorods for tumor theranostic applications. They showed good biocompatibility and high efficiency of these nanostructures in the NIR photothermal therapy of tumors. Furthermore, the contrast efficiency of PEGylated tungsten oxide nanorods was four times higher than that of the approved CT contrast agent Iohexol [17]. Wen et al. synthesized ultra-small biocompatible WO_3 nanodots with an outstanding X-ray radiation sensitization effect, which can be suitable for multi-modal CT-tumor imaging and photoacoustic imaging, as well as for two-way cancer treatment combining both photothermal therapy and radiation therapy [18]. Guo et al. developed a novel multifunctional theranostic system based on Cs_xWO_3 tungsten bronze nanorods (NRs). The surface of Cs_xWO_3 NRs was coated with polyelectrolyte multilayers using the layer-by-layer (LbL) technique, which improved the biocompatibility and uptake of these NRs. These Cs_xWO_3 NRs showed strong X-ray attenuation, strong NIR absorbance, and were successfully used for enhanced CT and PET imaging [19].

The issues of biocompatibility and long-term toxicity, and the

* Corresponding author at: Kurnakov Institute of General and Inorganic Chemistry of the Russian Academy of Sciences, Moscow 119991, Russia.
E-mail address: van@igic.ras.ru (V.K. Ivanov).

https://doi.org/10.1016/j.msec.2019.110494
Received 18 July 2019; Received in revised form 5 November 2019; Accepted 25 November 2019
Available online 26 November 2019
0928-4931/

mechanisms of biological activity of tungsten oxide nanoparticles, remain poorly understood. Thus, when considering WO_3 nanoparticles as a promising nanotheranostic agent, the molecular mechanisms of their cytotoxic effects on normal and cancer cells should be clarified. In this study, we thoroughly investigated the mechanisms of cytotoxicity of PVP-stabilized WO_3 nanoparticles in normal human mesenchymal stem cells and transformed human MNNG/Hos osteosarcoma cells. WO_3 nanoparticles were shown to possess highly selective cytotoxicity for normal and cancer cells. The expression of 96 key genes responsible for cell redox regulation was analyzed upon incubation with WO_3 nanoparticles, and the possible nature of WO_3 cytotoxic action is discussed.

2. Experimental section

2.1. Synthesis and characterization of tungsten oxide nanoparticles

Ultra-small hydrated tungsten oxide nanoparticles were synthesized by the processing of tungstic acid in the presence of polyvinylpyrrolidone (PVP K-30, average mol. wt. 40,000) as a template, stabilizer and growth regulator [20]. Tungstic acid was prepared by an ion-exchange method using sodium tungstate (Na_2WO_4) solution and strongly acidic cation exchange resin (Amberlite® IR120). Briefly, ion exchange resin (in hydrogen form) was swelled in water and loaded into a 200 mL glass column. Then, 100 mL of 0.05 M sodium tungstate solution was passed through the column dropwise and PVP (4 g) was added to the obtained eluent; the solution was then placed in a flask and stirred for 4 h under reflux. A clear sol of hydrated WO_3 was thus formed, as evidenced both by the appearance of a UV-absorption band at 325 nm and a Tyndall cone. The concentration of the as-prepared sol was measured gravimetrically; for cell experiments, the sol was diluted to 0.1–25.0 mg/mL concentrations. UV–vis spectra were registered using an Ocean Optics QE65000 spectrometer. The measurements were carried out with stirring at 37 °C. Prior to measurements, the sol was diluted to 0.1 g/L concentration. The hydrodynamic diameter and the ζ-potential values were measured using a Zetasizer Nano ZS analyzer (Malvern Instruments Ltd., UK). High-resolution transmission electron microscopy (HR-TEM) analysis was performed using a Libra 200 MC microscope (Zeiss, Germany). TEM images were recorded on a CCD camera (Gatan, USA) with a matrix size of 4096 × 4096 pixels.

2.2. Cell culture

The experiments were performed using a culture of primary human mesenchymal stem cells (hMSc) derived from the third molar bud, extracted from a healthy 16-year-old patient for orthodontic indications, and an MNNG/HOS human osteosarcoma cell line. The cells were cultivated in a DMEM/F12 (1:1) medium containing 10% of fetal bovine serum (FBS), 50 μg/mL of penicillin, 50 μg/mL of streptomycin and 1% of L-glutamine, at 37 °C in a humid atmosphere, comprising 95% air and 5% CO_2. The cells were seeded at a density of 30,000–35,000/cm^2. 6 h after cell attachment, the medium was replaced by a medium containing WO_3 NPs in different concentrations (0.1–25 mg/mL). In the control experiments, the cells were cultured without WO_3 NPs. The pH level of cultural media was measured by an Ohaus ST2100-B pH meter. The culture medium was collected and centrifuged at 5000 rpm for 5 min, and then the pH level of the supernatant was measured.

2.3. ICP-AES analysis

The content of WO_3 nanoparticles in the cells was determined by inductively coupled plasma atomic emission spectroscopy (ICP-AES) using a Thermo Scientific iCAP 6300 Duo spectrometer.

To prepare the samples for the analysis, the cells (MNNG/Hos and hMSc) were plated at a density of $3 \cdot 10^4$/cm^2 in 6-well plates in a DMEM/F12 cultural medium with 10% bovine serum. After 4 h incubation, WO_3 NPs (10 or 25 mg/mL) were added to the cells. After 24 h incubation, the cells were washed three times with HBSS and collected for analysis. Cell suspensions were placed in glassy carbon crucibles, and then 2 mL of nitric acid (65%) and 0.5 mL of hydrogen peroxide (30%, without stabilizer) were added. The solutions were heated on a ceramic tile to 150 °C and evaporated to dryness. Then 1 mL of perchloric acid (50%) and 0.5 mL of hydrofluoric acid (40%) were added to the obtained residues. The mixtures were heated to 150 °C until the complete dissolution of the residues. Then the temperature was raised to 210 °C to remove excess hydrofluoric acid. The solutions were transferred to 10 cm^3 polymer tubes, and the total weight of the solutions was adjusted to 10.0 g with deionized (18 MΩ) water. A control sample was prepared in the same way but WO_3 nanoparticles were not added to the cells.

The calibration of the spectrometer was performed using an ICP-MS-68B-B multi-element standard solution diluted to 0.200 or 1.00 mg/kg. The power supplied was 1150 kW; integration time for each measurement was 15 s; the sample was fed through a capillary (diam. 0.64 mm, 50 rpm); axial plasma survey was used. For the analysis, tungsten lines at 207.911 nm; 224.875 nm; 239.709 nm were used. The results were averaged over three analytical lines.

2.4. MTT assay

The activity of mitochondrial and cytoplasmic dehydrogenases in living cells was determined using an MTT assay based on the reduction of a colorless tetrazolium salt (3-[4,5-dimethylthiazol-2-yl]-2,5-diphenyltetrazolium bromide, MTT). The MTT assay was performed upon 24, 48, and 72 h of incubation of the cells with WO_3 nanoparticles.

2.5. LDH assay

LDH assay estimates the concentration of the cytoplasmic enzyme lactate dehydrogenase, which is found in the culture medium in cases of cell membrane damage. Cells were seeded in 96-well plates and cultured in an atmosphere containing 5% CO_2, at 37 °C. 6 h after cell seeding, the medium was replaced with the medium containing WO_3 NPs in different concentrations (0.1–25 mg/mL). Cells without the addition of NPs were used as a negative control. Triton X-100 (10 μL) was used as a positive control. The level of lactate dehydrogenase (LDH) was determined in the culture medium 72 h after the addition of nanoparticles, according to the manufacturer's protocol (Thermo Scientific™ Pierce™ LDH Cytotoxicity Assay Kit).

2.6. Analysis of proliferative activity

Cells were seeded in 24-well plates. 6 h after cell seeding, WO_3 NPs were added to the cells at various concentrations (0.1–25 mg/mL); 24, 48, and 72 h after the addition of the nanoparticles, cells were removed with trypsin/versene solution and counted in Goryaev's chamber.

2.7. Live/dead viability assay

To evaluate the cytotoxic effects of WO_3 nanoparticles, a Live/Dead Viability Kit (Invitrogen, Life Technologies) was used. Cells attached to the 96-well plate were processed according to the manufacturer's protocol, and visualized, 25 min after adding the dye, with a Zeiss Axiovert 200 fluorescence light microscope coupled with a Canon A620 digital camera. The green signal (SYTO 9 λ = 485/498 nm) characterized the live cells and the red signal (propidium iodide λ = 535/617 nm) characterized the dead cells. For each cell group, four fields in each well were examined.

2.8. Mitochondrial membrane potential measurement

Mitochondrial membrane potential (MMP) was determined using

fluorescence microscopy. JC-1 dye accumulates in the mitochondrial membrane in a potential-dependent manner. The high potential of the inner mitochondrial membrane facilitates the formation of the dye aggregates (J-aggregates), with both excitation and emission shifted towards red light (530 nm/590 nm) when compared with that for JC-1 monomers (485 nm/538 nm). The cells were seeded into 96-well tissue culture plates (Greiner) at a density of 5×10^4 cells/well in 100 μL culture medium, and cultured in a CO_2 incubator at 37 °C for 24, 48, and 72 h. The cells were pre-incubated with 5 μM JC-1 in the HBSS in a CO_2 incubator at 37 °C for 30 min. Next, the cells were washed twice with HBSS and analyzed using a Zeiss 200M inverted fluorescence microscope at 200× magnification. The results are shown as a ratio of fluorescence intensity measured at 530 nm/590 nm (aggregates) to that measured at 485 nm/538 nm (monomers).

2.9. Fluorescent staining of cell nuclei with Hoechst 33342

The cells were cultured in 96-well plates, as described above. After 24, 48, and 72 h of culturing with WO_3 NPs, the cells were washed with HBSS and stained for 20 min with Hoechst 33342 (1 μg/mL). Images of stained cells were captured by fluorescence microscopy and the percentage of apoptosis was calculated by cell counting (> 600 cells scored per group).

2.10. Detection of intracellular reactive oxygen species (ROS)

The level of intracellular ROS was determined using dichlorodihydrofluorescein (DCF) and dihydroethidium (DHE). DCF is a dye that diffuses through the lipid membrane into the cell and is subsequently oxidized by intracellular ROS (preferably by hydrogen peroxide), with the formation of highly fluorescent dichlorofluorescein. Upon treatment of hMSc and MNNG/Hos cells with WO_3 NPs, the medium was aspirated and cells were washed twice with HBSS and incubated in 1 mL of medium without serum. DCF and DHE were added at a final concentration of 40 μM and 10 μM, respectively. After 20 min incubation at 37 °C, the cells were washed once with HBSS and kept in a fresh HBSS. The quantitative analysis of fluorescence was performed using a Tecan 200 PRO plate reader (485 nm/520 nm). The average fluorescence intensity was measured in five randomly chosen fields at 200× magnification, n = 4.

2.11. Detection of apoptosis by Yo-Pro-1 dye

To evaluate the number of apoptotic cells upon incubation with WO_3 nanoparticles, a YO-PRO-1 dye (1 μM) was used. YO-PRO-1 dye has found a niche in identifying apoptotic cells because apoptotic cells are permeable to this dye, but not permeable to propidium iodide, which is used for staining dead cells. Cells attached to the 96-well plate were stained according to the manufacturer's protocol, and visualized, 25 min after adding the dye, with a Zeiss Axiovert 200 fluorescence-light microscope coupled with a Canon A620 digital camera. For each cell group, three fields in each well were examined.

2.12. RT-PCR

Reverse transcription was performed with a Sileks kit (Russia), using an oligodT primer according to the manufacturer's protocol. The produced cDNAs served as a real-time PCR matrix. For the PCR reaction, a mixture was used with SYBR Green dye (Syntol, Russia). We used the CFX-96 amplifier (BioRad, USA) or the ABI 7500 Fast Real-Time PCR System (Applied Biosystems, USA). The expression of 96 genes responsible for key cell processes (Table 1) was thus determined.

The analyzed genes were selected from the database http://www.sabiosciences.com/ for PCR profiling of different biological processes. The level of gene transcription was normalized by the levels of expression of housekeeping genes β-*actin*, *rplp0* (ribosomal protein, large, P0) and *gapdh* (glyceraldehyde-3-phosphate dehydrogenase). The gene-specific primers were selected in the Primer Express program (Applied Biosystems, USA). Each measurement was made twice (internal repetition) and averaged for two independent samples. A sample without reverse transcription stage was used as the control. The obtained expression data were analyzed using online services http://www.sabiosciences.com/, mayday-2.14 software (Center for Bioinformatics, Tübingen, Germany) and Genesis software.

2.13. UV irradiation

Cells were irradiated for 20 min with the UV light (pulsed UV lamp with a continuous spectrum of radiation in the range of 200–700 nm, 50 W cm^{-2}, Melitta, Alpha 05, Russia); the cells in the control group were not irradiated. In the next step, cells were grown for an additional 24 h in the CO_2 incubator at 37 °C, under a humidified atmosphere of 5% CO_2 (v/v), and were subsequently sampled for morphology determination, live/dead assay and MTT assay. To confirm the WO_3 sol's photochromic properties, it was exposed to UV light (312 nm) in a BLX-E312 chamber for 10 min. To study the pH-dependent photochromic properties of WO_3 sol, it was irradiated for 0–20 min by a black light bulb (DeLux EBT-01 26 W BLB, λ_{max} 370 nm).

2.14. Statistical analysis

The experiments were conducted in 3–4 repetitions, with three independent repetitions for each WO_3 NPs concentration. Experimental results were compared with the control. Statistical analysis was performed using the methods of variation statistics. We determined the mean values and the standard deviation of the mean. The significance of differences between the groups was determined using Student's *t*-test. The obtained data were processed using GraphPad 6.0 and Microsoft Excel 2007 Software.

3. Results and discussion

According to HR-TEM data (Fig. 1a), the sample consisted of WO_3 nanoparticles of approximately 1 nm in size. According to DLS data, the WO_3 sol contained particles of various sizes (2.0 ± 1.0 nm, 7.0 ± 3.8 nm, 209.0 ± 73.0 nm) (Fig. 1b). It can be assumed that the sol contains both individual WO_3 nanoparticles with a hydrodynamic diameter of about 2 nm, and WO_3/PVP complexes of larger size. The second maximum in the WO_3 sol particle size distribution presumably corresponded to PVP colloid particles, as the position of this maximum matched the position of a single maximum typical for pure PVP solution. In turn, colloid particles larger than 100 nm can be formed upon WO_3 interaction with PVP molecules. The presence of PVP molecules containing no WO_3 nanoparticles in the sol was also confirmed by ζ-potential measurements (Fig. 1c). The observed complex ζ-potential distribution is typical for colloid systems containing both electrostatically stabilized particles (a broad distribution of the negative values) and uncharged sterically stabilized moieties (a relatively narrow peak at −7 mV).

According to UV–visible spectroscopy (Fig. 1d), the shape and the position of the absorption peak of the PVP-stabilized tungsten trioxide sol differed from that of the pure PVP solution, indirectly proving the formation of a PVP complex with tungsten trioxide nanoparticles. Moreover, the abrupt change in the position and shape of the absorption peak of the PVP-stabilized WO_3 sol upon UV irradiation demonstrated its good photochromic properties. The coloration/discoloration process was reversible, and the absorption spectrum of the sol returned to its initial state after the turning off of the UV light. The whole discoloration process took about 10 min. The photochromism of tungsten oxide nanoparticles, promoted by electron-donor nitrogen atoms in PVP, has been extensively discussed elsewhere [20,21]. The mechanism of the color change is most probably connected to the charge-transfer

Table 1
Selected gene groups for RT-PCR analysis.

Gene	Functions	Gene	Functions	Gene	Functions
KAT2A	Chromatin and chromosome modulators	HSPA9	Self-renewal markers	FOXA2	Stemness reduction markers
RB1		SOX1		PTCH1	
				CD34	
TERT		BMP7		AXL	Cell migration markers
DHH	Regulators of cell division symmetry	DNMT1		IL8	
NUMB		APC	Stemness maintenance (Wnt signaling)	SNAI1	
PARD6A		AXIN		TWIST1	
HDAC2	Stemness maintenance (Notch signaling)	MSX1		ZEB1	
JAG1		CCND1	Proliferation markers	KLF4	Pluripotency markers
NOTCH1		CDK4		MYC	
NOTCH2		CDC6		NANOG	
ALPL		WEE1		POU5F1	
BGLAP	Markers of MSCs and their differentiation	CCNA2		SOX2	
BMP1		AURKB		NOS2	Anti-apoptotic markers
BMPR1A		CCNB2		BCL2	
COL1A1		CUL1		BIRC3	
COL3A1		SKP2		MCL1	
EGFR		CCNB1		TRAF2	
FGF-2		CDK7		ATG3	Autophagy markers
FGFR1		CDKN1B		ATG12	
IGF1		CDKN2A		NFKB1	
IGFR1		CDKN2B		RPS6KB1	
		TP53		CCDC103	Necrosis markers
RUNX2		MCM2		FOXI1	
SMAD2		LIN28B		JPH3	
SMAD4		FOXP1	Markers of asymmetric cell division	RAB25	
SMAD5		SIRT1		BAX	Pro-apoptotic markers
SPP1		WNT1		CD40	
TGFBR1		ALDH1A	Stemness markers	CFLAR	
TNF		CD44		FAS	
VDR		GATA3		TNFRSF10A	
		ITGA6			
		ITGB1			

process between oxide nanoparticles and the organic matrix, as proposed by Jing et al. [22]. During the coloration process, the valence change $W^{+6} \rightarrow W^{+5}$ occurs [23], and the bleaching process is initiated by oxygen [21]. Importantly, the formation of the ligand-to-metal charge transfer complex results in almost reversible photochromism, and can lead to the formation of ROS, namely hydroxyl-radicals [24]. The bleaching of the composite may occur through electron transfer from W^{+5} to the oxygen molecule, forming other ROS, namely superoxide anion-radicals: $O_2 + W^{+5} \rightarrow O_2^- + W^{+6}$ [18].

In our study, we investigated a wide range of WO_3 NPs concentrations, but in the further experiments we used only the concentrations above 0.1 mg/mL (1–25 mg/mL), since lower concentrations (1–100 μg/mL) did not produce any effect (Fig. S1). Analysis of the dehydrogenase activity (MTT assay) of both cell cultures (hMSc and MNNG/HOS) upon incubation with WO_3 NPs showed that hMSc cells were much more resistant to the toxic effect of WO_3 nanoparticles (Fig. 2). After 24 h, the viability of hMSc was reduced by 20–30% in the presence of high concentrations of WO_3 NPs (25, 15, 10 mg/mL), while the viability of MNNG/HOS osteosarcoma cells decreased by 50%. After 72 h, the viability of hMSc decreased significantly (by 50% and more) only in the presence of a higher concentration of WO_3 NPs (25 and 15 mg/mL), while lower concentrations of WO_3 NPs (10, 5 and 1 mg/mL) did not cause notable changes in their viability. Meanwhile, the viability of osteosarcoma cells was below 50%, even upon treatment with 5 mg/mL WO_3. Different cell cultures demonstrated different dynamics of the response to the toxic effect of WO_3 NPs. MNNG/HOS cells showed high sensitivity to WO_3 concentrations higher than 5 mg/mL after 24 h of culturing, while hMSc demonstrated less viability decrease in this time slot. Moreover, after 24 h of cultivation, hMSc showed a dose-dependent loss of viability, whereas MNNG/HOS demonstrated resistance to WO_3 NPs concentrations of 0.1, 0.5 and 1 mg/mL, and high sensitivity to high WO_3 concentrations (from 5 to 25 mg/mL). One of the possible mechanisms of this effect is the different proliferative activity of the tested cell cultures, different rates of nanoparticles' endocytosis, and further intracellular localization [25]. Additionally, we used inhibitory analysis to confirm the cytotoxic effect of WO_3 NPs. Two types of pharmacological inhibitors – amantadine inhibitors (500 μM) for caveolin-dependent endocytosis pathways and amiloride (1 mM) for clathrin-dependent endocytosis pathways – were used. Pretreatment of cell cultures with endocytosis inhibitors prevented the cytotoxic effect of WO_3 NPs in both types of cells. This confirms that the cytotoxic effect of WO_3 NPs takes place in the cells just upon the uptake of NPs (Fig. S2). Thus, using inhibitory analysis, we demonstrated the caveolin/clathrin dependent uptake of WO_3 NPs. Earlier, a molecular mechanism of the interaction of nanocrystalline tungsten oxide with human genomic DNA was investigated. It was shown that WO_3 NPs were able to interact with DNA by electrostatic forces through phosphate bonding. Additionally, WO_3 NPs inhibited Taq polymerase, and this can also be considered as one of the cytotoxic mechanisms for this type of nanoparticle [26].

Quantitative analysis of dead cells in the MNNG/Hos cell line using a live/dead assay showed a slight increase in dead cells' quantity (propidium iodide positive cells) after 24 h of incubation with all the concentrations of WO_3 NPs (5, 10, 15 and 25 mg/mL), while hMSc began to die only when treated with the highest concentrations of WO_3 NPs (15 and 25 mg/mL) (Fig. 3b, c). After 72 h, the number of dead cells for the MNNG/Hos cell line was 100%, for all concentrations of WO_3 NPs, starting from 5 mg/mL. In turn, hMSc showed 100% death only after incubation with 15 mg/mL and higher concentrations of WO_3 NPs. The qualitative analysis has clearly demonstrated that the treatment of MNNG/Hos cells with WO_3 NPs resulted in a high percentage of cell death for any WO_3 concentration used, while hMSc died within 72 h only when treated with high concentrations of WO_3 NPs (15 and 25 mg/mL) (Fig. 3).

Previously, it has been shown that tungsten oxide nanoparticles are capable of generating hydroxyl radicals [27]. Hydroxyl radicals are

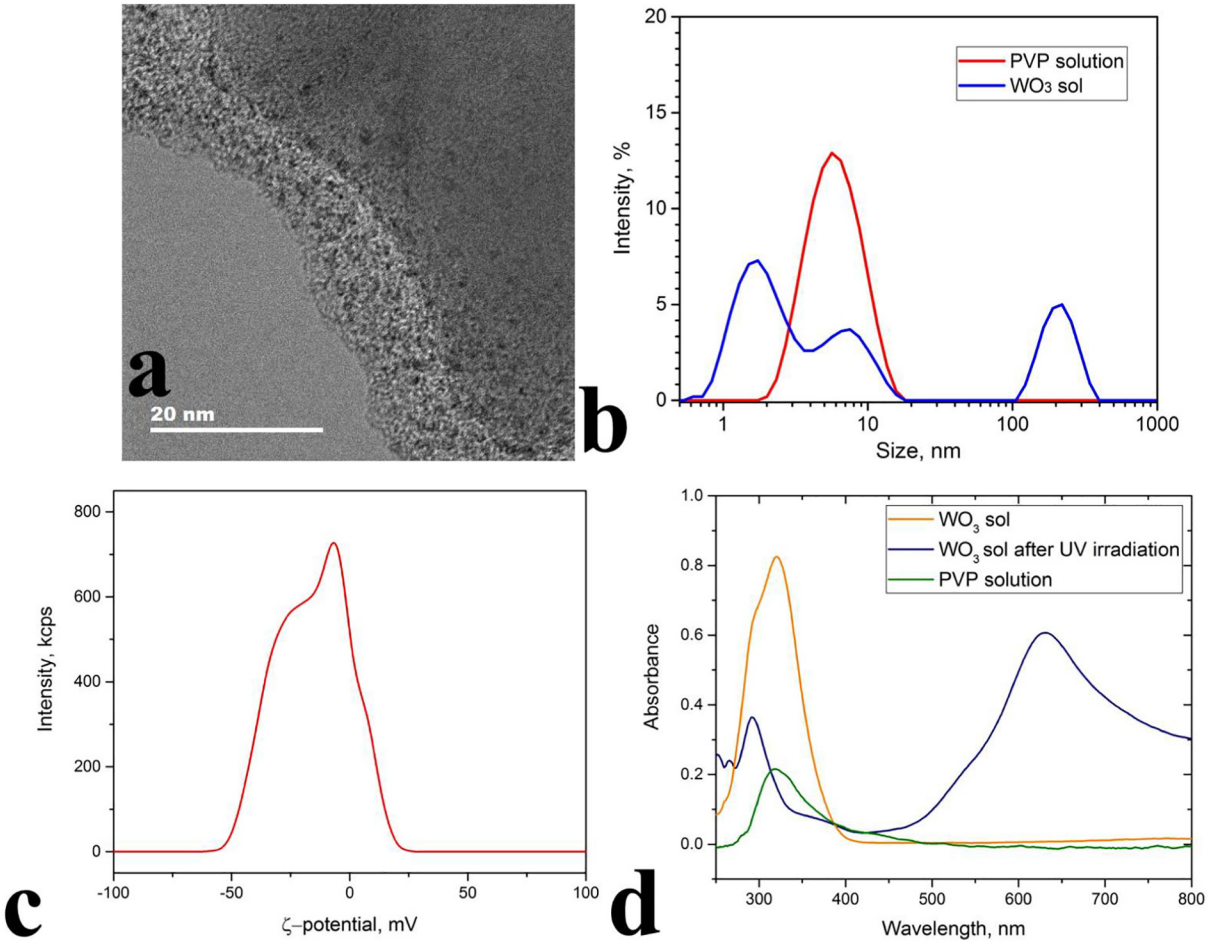

Fig. 1. TEM image of PVP-stabilized WO_3 nanoparticles (a). Size distribution and ζ-potential of the PVP-stabilized WO_3 sol (b, c). UV spectra of the PVP-stabilized WO_3 sol (yellow), sol after UV irradiation (blue) and PVP solution (green) (d). (For interpretation of the references to color in this figure legend, the reader is referred to the web version of this article.)

among the most powerful oxidizing agents that can react with biomacromolecules such as amino acids, nucleic acids, and lipids, and promote double bond scission, secondary ROS formation (for example, H_2O_2), hydrocarbon degradation, and the generation of long-living protein radicals [28–30]. Due to the ability of WO_3 NPs to generate a hydroxyl radical, the major cause of cell death can be associated with lipid peroxidation and damage to cell membranes, which allows for intense cell staining with propidium iodide. To check this assumption, we used the LDH assay, which is based on measuring free lactate dehydrogenase in a culture medium.

Normally, lactate dehydrogenase is absent in the culture medium, but when the cell membranes are damaged, it is released into the culture medium, where its concentration can be measured. Fig. 4 shows that even low concentrations of WO_3 NPs (0.5 and 1 mg/mL) cause an increase in the level of free lactate dehydrogenase in the MNNG/Hos cell line. Concentrations of 5 mg/mL and higher reduce significantly the viability of osteosarcoma cells (up to 20%), whereas normal cells die in a dose-dependent manner, and only 15 and 25 mg/mL concentrations of WO_3 NPs are highly toxic to them.

Analysis of the growth curves of cell cultures in the presence of WO_3

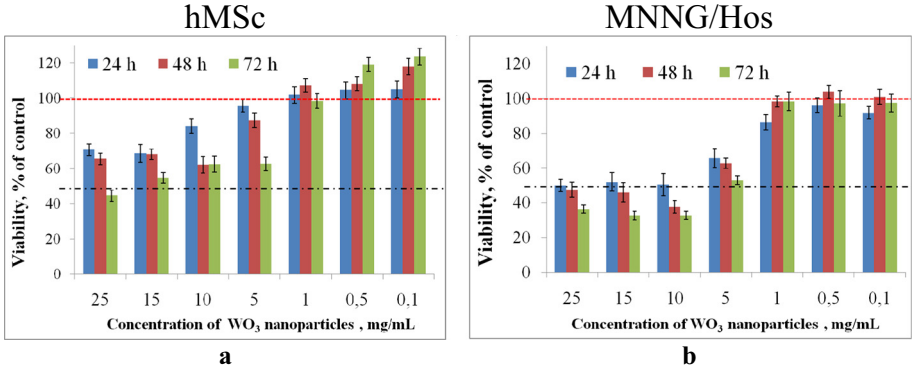

Fig. 2. Cell viability of hMSc (a) and MNNG/HOS (b) cells as determined using MTT assay after 24, 48, and 72 h incubation with different concentrations (0.1–25 mg/mL) of WO_3 NPs. Results are shown as the mean ± SE (n = 6).

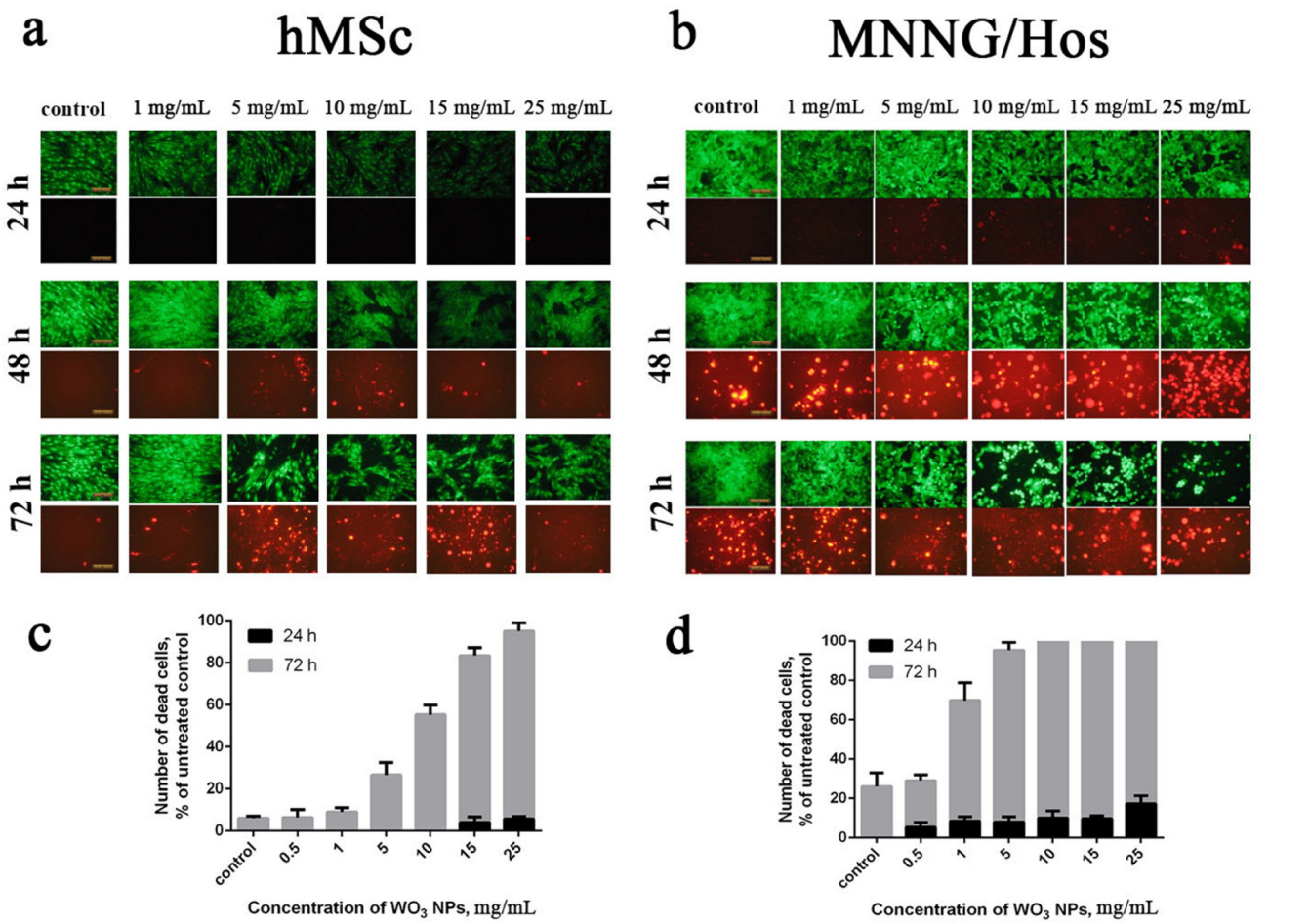

Fig. 3. Live/dead viability assay after 24, 48, and 72 h of incubation with WO_3 NPs. Qualitative (a, b) and quantitative (c, d) analysis of cell viability after incubation with different concentrations (0.5–25 mg/mL) of WO_3 NPs. All cells were stained green and only dead cells were stained red. Scale bars are 20 μm in all the images. (For interpretation of the references to color in this figure legend, the reader is referred to the web version of this article.)

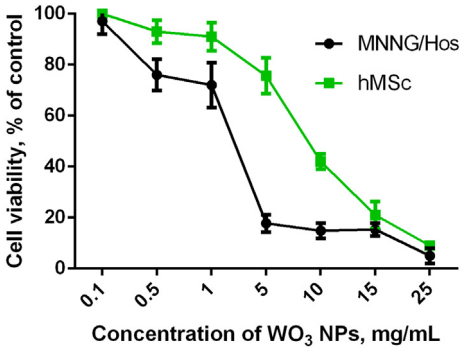

Fig. 4. LDH assay of MNNG/HOS and hMSc after 72 h culturing with WO_3 NPs. The data are presented as viability as a % of untreated control (without WO_3 nanoparticles).

NPs shows that the proliferation of MNNG/Hos cells is inhibited by all the concentrations of WO_3 NPs, while for normal hMSc, only concentrations above 10 mg/mL are inhibitory (Fig. 5). The slowing down of proliferation is directly related to the disturbance of intracellular metabolism, due to the development of oxidative stress. Additionally, we performed a morphological analysis of the actin cytoskeleton, which confirmed the destructive state of the cytoskeleton at high concentrations of WO_3 NPs, especially for cancer cells (Fig. 6). Earlier, Paget et al. showed that ROS generation by tungsten carbide-cobalt (WC-Co) nanoparticles can lead to DNA double-strand breaks, cell cycle arrest and/or mitotic catastrophe [31].

The selective action of WO_3 NPs on different types of cells can be considered promising for the design of new theranostic agents, since their activity against cancer cells is much higher than their activity against normal cells. It should also be noted that, apparently, one of the mechanisms of such selective cytotoxicity may be differences in uptake efficacy. For example, it has previously been shown that cells can absorb WC-Co nanoparticles differently. Internalization of WC-Co NP was lower overall in A549 cells compared with Caki-1 and Hep3B cells. In addition, it has been shown that A549 cells have the capability of uptake and faster release of inorganic NPs [32].

We analyzed the uptake of WO_3 NPs by MNNG/Hos and hMSc cells using ICP-AES. The mean cellular uptake of WO_3 NPs, expressed as picogram of tungsten per cell, is summarized in Table 2. Data obtained indicate that the increase in the concentration of WO_3 NPs in the incubation medium resulted in the higher uptake of WO_3 by the cancer cells while the uptake of the nanoparticles by normal cells remained nearly the same.

To analyze the possible mechanisms of WO_3 NPs' cytotoxicity, we carried out a qualitative and quantitative morphological analysis of cell nuclei after incubation with WO_3 nanoparticles for 24, 48, and 72 h. Considering the high redox-activity of WO_3 NPs, we assumed that the major cause of cell death could be apoptosis induced by a high level of intracellular ROS. The first morphological evidence of apoptosis is the detachment of the cell, which loses its adherence, while its cytoplasm and plasma membrane start to convolve, showing extensive and rapid blebbing. This blebbing can be observed for several hours, and is

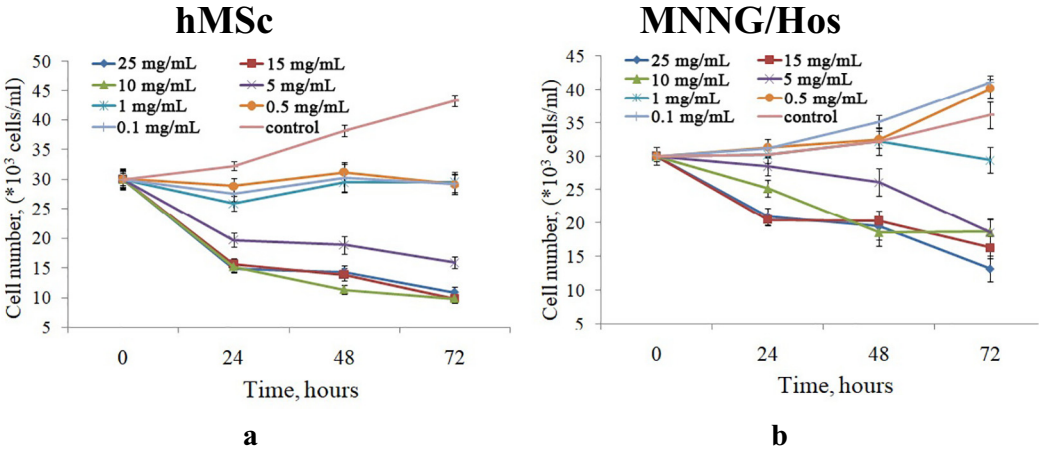

Fig. 5. Proliferation of hMSc (a) and MNNG/Hos (b) cells after 24, 48, and 72 h incubation with different concentrations (0.1–25 mg/mL) of WO_3 NPs.

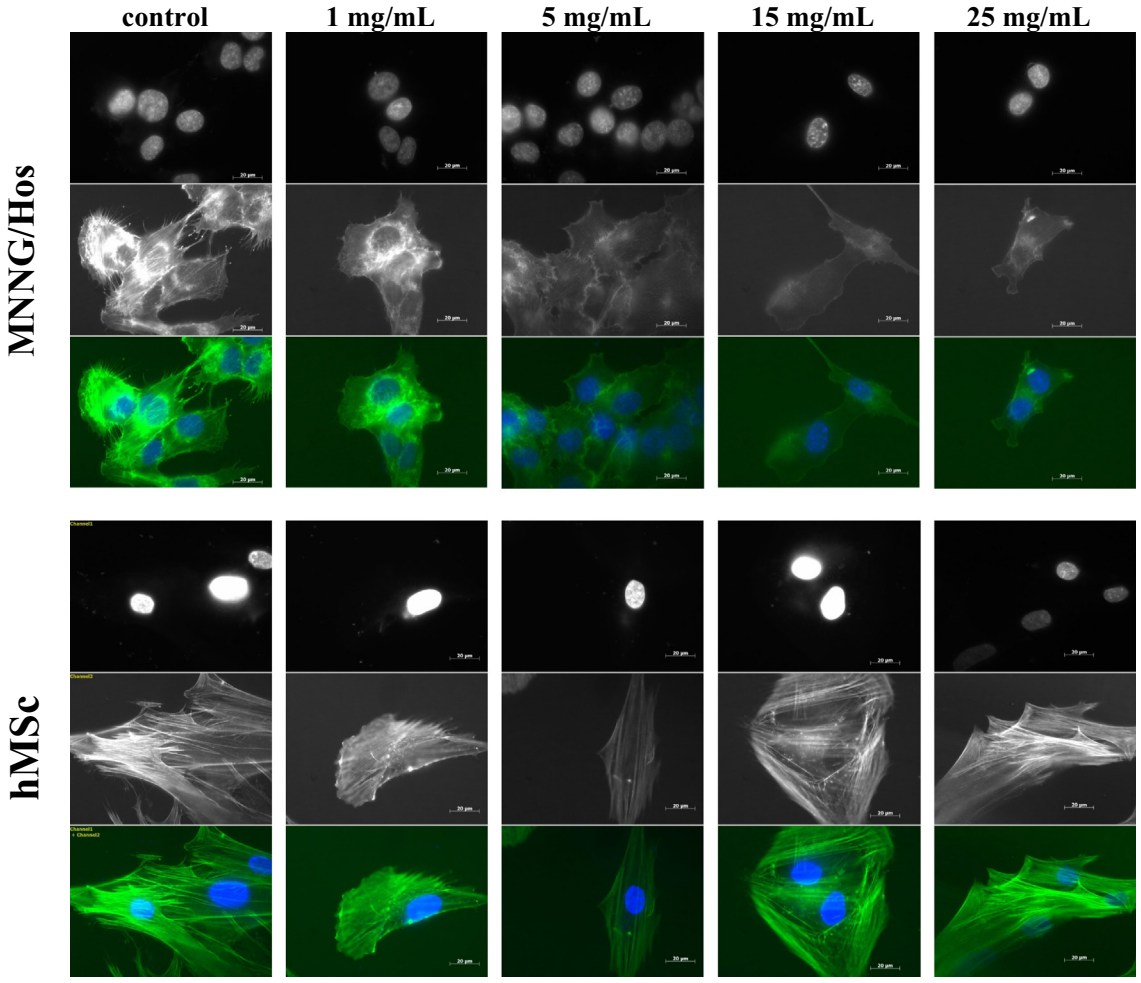

Fig. 6. Analysis of cytoskeleton distribution and cell morphology after the cells' exposure to PVP-WO_3 nanoparticles. Actin cytoskeleton and nucleus were stained with FITC conjugated phalloidin (green) and Hoechst 33342 (blue), respectively. Scale bar is 20 μm. (For interpretation of the references to color in this figure legend, the reader is referred to the web version of this article.)

followed by a vast reorganization of the organelles and cytoskeleton. At the nuclear level, chromatin becomes highly condensed, and the nucleus is usually fragmented in small micronuclei. Finally, the cell is divided into several fragments that are called apoptotic bodies, which will be phagocytosed by neighboring cells or will degenerate *via* secondary lysis, leading to the loss of the cell content to the surrounding media [33]. Primary morphological analysis of the cell nuclei after incubation with WO_3 nanoparticles was carried out by staining cells with the fluorescent dye Hoechst 33342 (Fig. 7). It should be noted that, at high WO_3 NPs concentrations, the intensity of nuclei fluorescence was reduced in both tested cell cultures. Considerable membrane blebbing, defragmentation and ruffling occur in MNNG/Hos cells after

Table 2
Cellular uptake of WO_3 NPs as measured by ICP-AES.

Concentration of WO_3 (mg/mL)	Tungsten content (pg/cell)	
	MNNG/Hos (cancer cell line)	hMSc (normal cell line)
10	4.2 ± 1.2	3.6 ± 1.1
25	15.0 ± 2.3	5.37 ± 1.6

24 h of incubation, with all tested concentrations of WO_3 NPs, while similar changes in hMSc nuclei are observed only after 48 h of incubation and only when using the highest concentrations (15 and 25 mg/mL) of WO_3 NPs. Fig. 7b shows that 1, 5, and 10 mg/mL concentrations of WO_3 NPs led to an increase in the proportion of cells with an altered nucleus in the osteosarcoma cell culture, while this effect is substantially less pronounced in stem cells.

Mitochondrial membrane potential (MMP) change is a hallmark for apoptosis [34]. Using the cationic dye JC-1, we investigated mitochondrial membrane potential in hMSc and MNNG/Hos cells after incubation with WO_3 NPs. Cells were treated with different concentrations of WO_3 NPs for 24, 48, and 72 h. The results are shown in Fig. 8. The data obtained indicate that higher concentrations (10, 15, and 25 mg/mL) of WO_3 NPs decrease MMP in both hMSc and MNNG/Hos cells. Microscopic images revealed that the red fluorescence intensity of JC-1 aggregates decreased, while the green fluorescence intensity of JC-1 monomers increased upon WO_3 NPs treatment in both cell lines, as compared to the untreated control cells. The resulting decrease in the red to green fluorescence ratio indicates the loss of mitochondrial membrane potential. Meanwhile, the response of the cells to the lower concentrations of WO_3 NPs was different. MNNG/Hos osteosarcoma cells showed a more significant reduction of MMP in comparison to normal hMSc cells ($p < 0.05$).

The apoptosis process typically takes 8–15 h, and using YO-PRO-1 dye, it can be reliably analyzed after 10 h [35]. Using YO-PRO-1 (Ex/Em 491/509 nm) as a marker of plasma membrane integrity, instead of propidium iodide, allows for a more accurate detection of early apoptotic cells [36]. Therefore, we estimated the number of apoptotic cells after 24 h of incubation with WO_3 nanoparticles (Fig. 9). The number of apoptotic cells in the hMSc after incubation with WO_3 nanoparticles was close to zero, while for the MNNG/Hos cells this parameter was significantly higher and increased in a dose-dependent manner.

It is well known that apoptosis can develop along extrinsic and intrinsic pathways. The extrinsic apoptosis pathway develops *via* activation of the TNF receptors family [37]. The intrinsic apoptosis pathway develops *via* mitochondrial dysfunction, due to a disturbance of oxygen metabolism or other destructive processes [38]. Taking into account the high catalytic activity of nanocrystalline tungsten trioxide, MMP collapse (Fig. 8), and a high intracellular ROS level (Fig. 10), we can assume that WO_3 nanoparticles initiate apoptosis *via* an intrinsic pathway due to intracellular oxidative stress.

Oxygen metabolism generates hydroxyl radicals (·OH), superoxide radicals (O_2·), and non-radical hydrogen peroxide (H_2O_2). Hydroxyl radicals are highly reactive and readily react with biological molecules such as DNA, proteins, lipids, *etc.*, causing their chemical modification. Superoxide radicals and H_2O_2 do not react with most biological molecules, but the presence of metal ions could catalyze the Haber-Weiss reaction, producing ·OH [39]. DCF, a ROS sensitive dye, and DHE, a specific superoxide indicator, were used to analyze ROS generation induced by WO_3 NPs in MNNG/Hos and hMS cells. Qualitative data indicate that, in WO_3 NPs-treated cells, dose-dependent ROS generation takes place (Fig. 10a, b). The overall ROS level (DCF staining) was

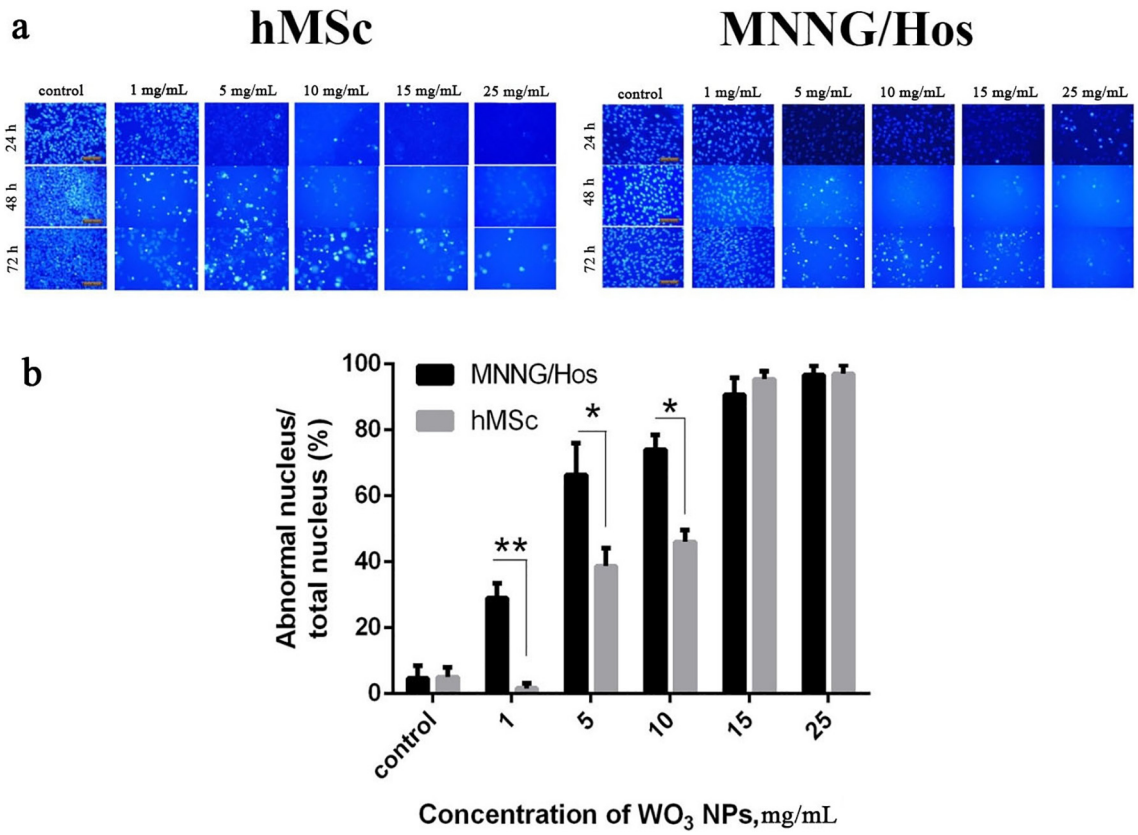

Fig. 7. The effect of WO_3 nanoparticles on the nucleic morphology of hMSc and MNNG/Hos cells: qualitative (a) and quantitative (b) analysis. Cells were incubated with WO_3 NPs for 24, 48, and 72 h, and then stained with Hoechst 33342 to detect apoptotic morphology. The graph shows the number of abnormal cell nuclei after 72 h incubation with WO_3 NPs.

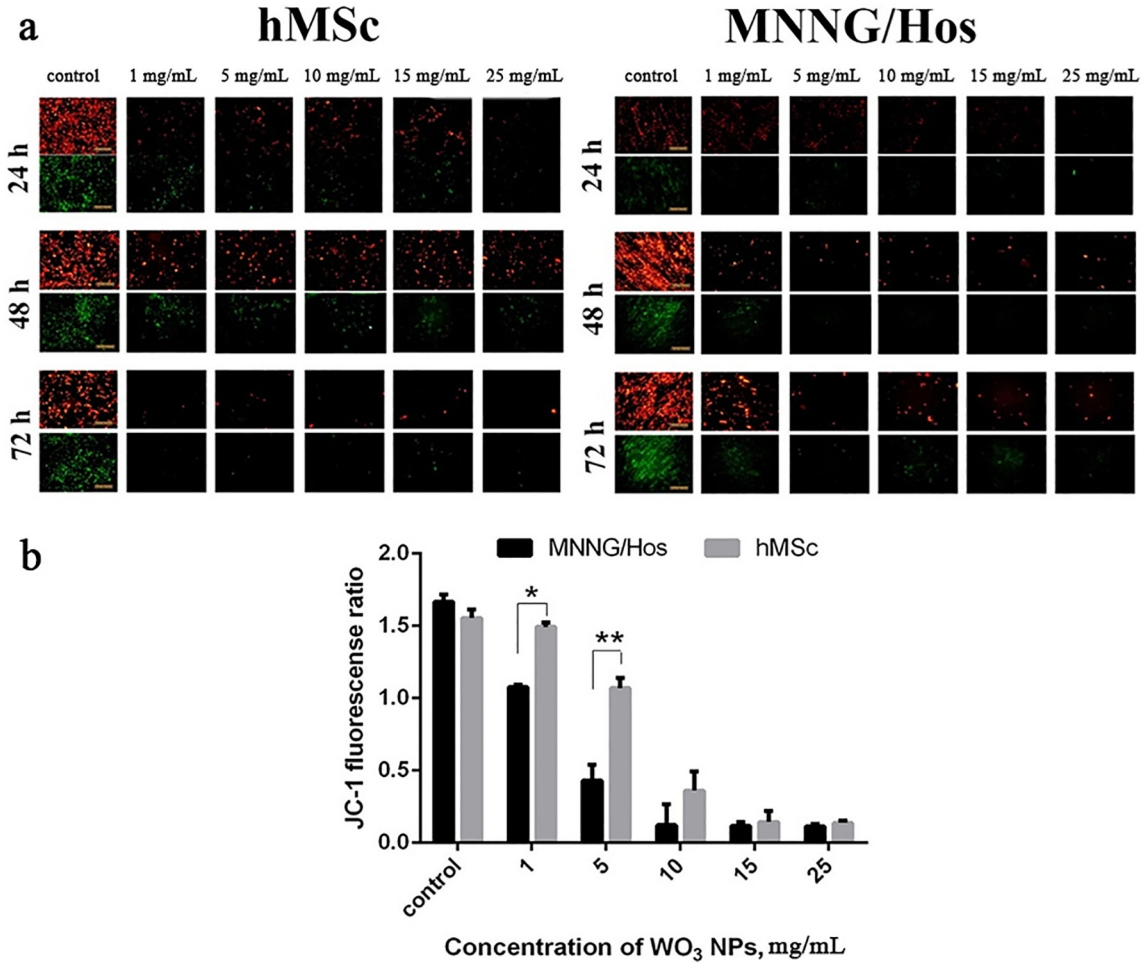

Fig. 8. The effect of WO_3 NPs on mitochondrial membrane potential (ΔΨm) in hMSc and MNNG/Hos cells: qualitative (a) and quantitative (b) analysis. Cells were incubated with WO_3 NPs and then stained with JC-1 to analyze ΔΨm. The ΔΨm was assessed as a ratio of JC-1 red/green fluorescence intensities. Qualitative assessment of the MMP after 72 h (a), quantitative assessment of the MMP after 72 h (b); *$p < 0.05$, **$p < 0.001$. (For interpretation of the references to color in this figure legend, the reader is referred to the web version of this article.)

higher in the MNNG/Hos cell line than in normal cells, starting at 2.5 mg/mL. It should be noted that the hydroxyl radical level (DHE staining) was higher in the MNNG/Hos cells, compared to normal cells after incubation with 5 and 10 mg/mL of WO_3 NPs. The highest concentrations of WO_3 NPs (15 and 25 mg/mL) led to a significant increase in the ROS level, so the differences between these cell types were not observed. Comparing these results and MMP levels (Fig. 8) after incubation with WO_3 NPs, one can assume that the main mechanism that triggers cell death is the apoptosis developed *via* the mitochondrial pathway. This result is in agreement with a previous study which indicated that tungsten-containing particles could generate a higher level of free radicals and induce greater oxidative stress [40].

For a more detailed analysis of the mechanisms of cell death upon WO_3 NPs incubation, we analyzed the gene expression of key genes at high concentrations of WO_3 nanoparticles (5, 15, and 25 mg/mL). Using the RT-PCR method, we examined the expression levels of 96 genes involved in ROS metabolism, apoptosis, necrosis, and autophagy. Gene expression levels are presented as a heat map (Fig. 11). Data presented show down-regulation for almost all 96 selected genes for osteosarcoma cells, regardless of the nanoparticles concentration, while for the normal cells, overexpression was dose-dependent. In cancer cells, overexpression is observed in only two genes (CCNA2 and MYC), which are responsible for proliferation. It should be noted that mutations of the MYC gene are found in many tumors, and this gene is permanently expressed, which leads to a disruption in the regulation of the activity of many other genes responsible for cell proliferation [41]. Therefore, the increased level of its transcription in comparison with the rest of the gene group is quite expected. In cancer cells, down-regulation of genes responsible for necrosis (FOXI1, JPH3, and RAB25) is also observed. Meanwhile, in the culture of normal cells, WO_3 NPs caused a change in gene expression in a dose-dependent manner for almost all groups of genes. Dose-dependent overexpression is observed for the NFKB1 gene, which encodes the DNA-binding subunit of the NF-κB protein complex, which is stimulated in the cell by numerous external and internal factors. Activated NF-κB is translocated into the nucleus and stimulates the expression of > 200 genes involved in many cellular functions, in particular in response to oxidative damage [42]. In addition, a notable increase in expression is observed among markers of MSCs and their differentiation (BGLAP, COL1A1, FGF-2, FGFR1, RUNX2).

A significant difference between normal and malignant cells was found in the expression levels of all the selected anti-apoptotic genes (NOS2, BCL2, BIRC3, MCL1). These genes showed 2–3 fold up-regulation in normal cells and down-regulation in malignant cells. The role of the B cell lymphoma 2 (BCL2) family of proteins in the rescue of both malignant and normal cells from programmed death (apoptosis) is well known [43]. Yassin et al. demonstrated the selective cytotoxicity of WO_3 nanoparticles to normal (VERO, MDCK, MRC5) and cancer (Caco2 and Hela) cells when the selectivity index reached 3.2 and 2.6 on colon and cervix cancer, respectively [44]. The selective toxicity of tungsten oxide nanoparticles was supposed to be due to their high oxygenation

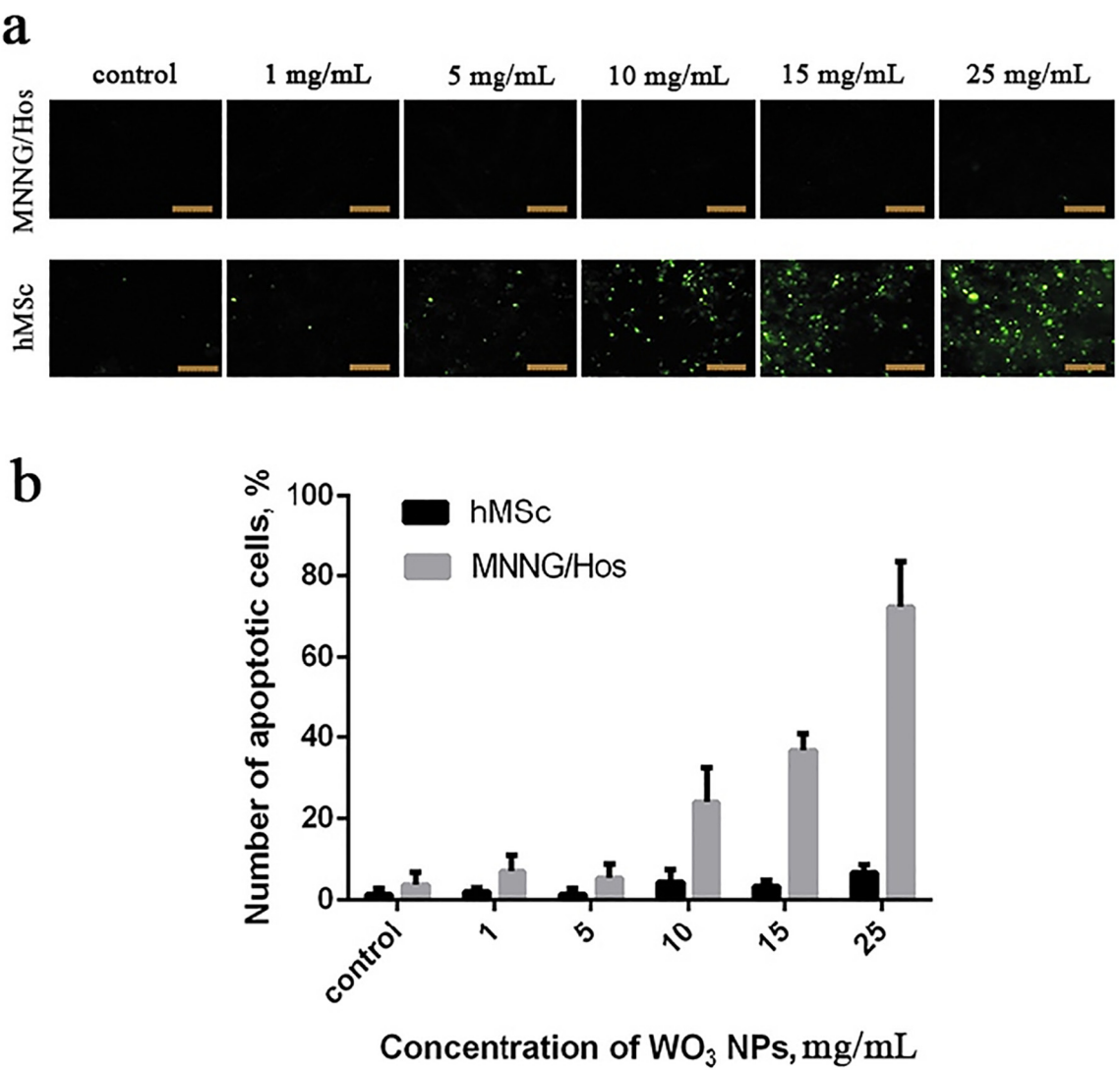

Fig. 9. Analysis of apoptotic cells using YO-PRO-1 dye after 24 h incubation with different concentrations of WO_3 NPs. hMSc and MNNG/Hos cells were stained by YO-PRO-1 (1 μM) and observed under a fluorescence microscope. Quantitative assessment of apoptotic cells was made by analyzing at least three fields from three different images.

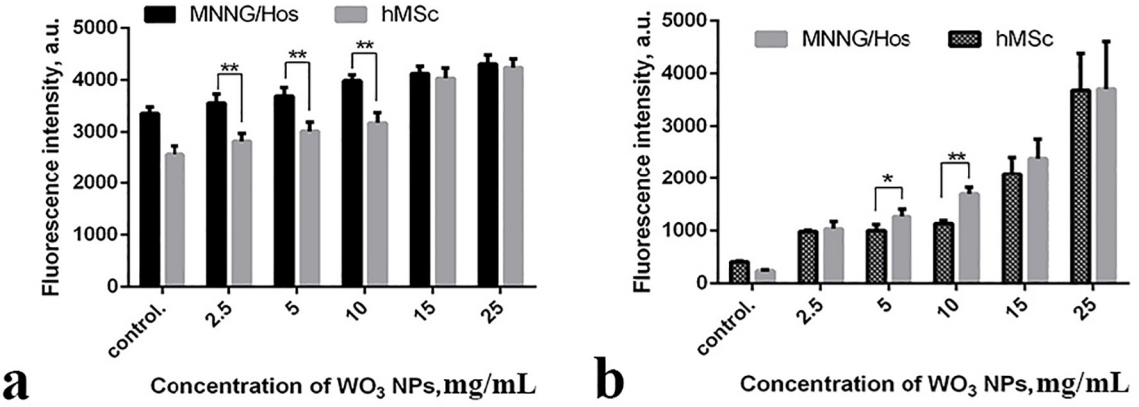

Fig. 10. The effect of various concentrations of WO_3 NPs on intracellular ROS accumulation after 24 h of incubation. Hydrogen peroxide detection by DCF dye (a), superoxide detection by DHE dye (b). Data are expressed as the mean ± SD of three identical experiments (n = 3). *p < 0.01, **p < 0.001.

and different oxygen sensitivity in normal and malignant cells. The results obtained by Yassin et al. indicate that tungsten oxide nanoparticles downregulated the expression of BCL2 (and MMP7) genes in cancer cells. In this way, normal cells acquire additional protection against apoptosis (including oxytosis), while the viability of cancer cells is significantly reduced. Importantly, based on Warburg cancer theory, all normal cells are aerobic, whereas all cancer cells are typically anaerobic, *i.e.*, high oxygenation is harmful to cancer cells but not to

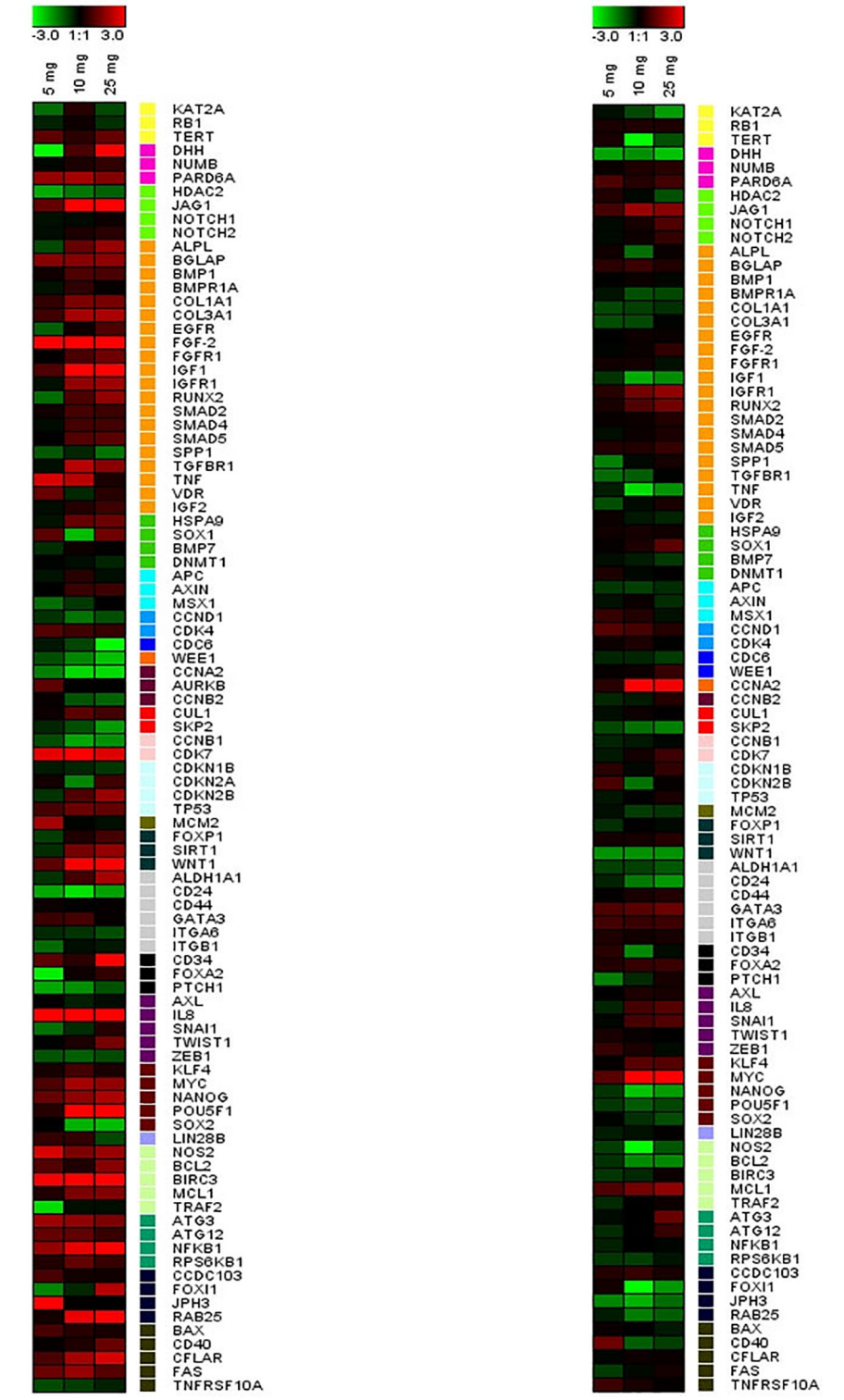

Fig. 11. Heat map of gene expression in hMSc and MNNG/Hos cells after 72 h incubation with WO_3 nanoparticles (5, 10 and 25 mg/mL). The intensity scale of the standardized expression values ranges from −3 (green: low expression) to +3 (red: high expression), with the 1:1 intensity value (black) representing the control (non-treated cells). (For interpretation of the references to color in this figure legend, the reader is referred to the web version of this article.)

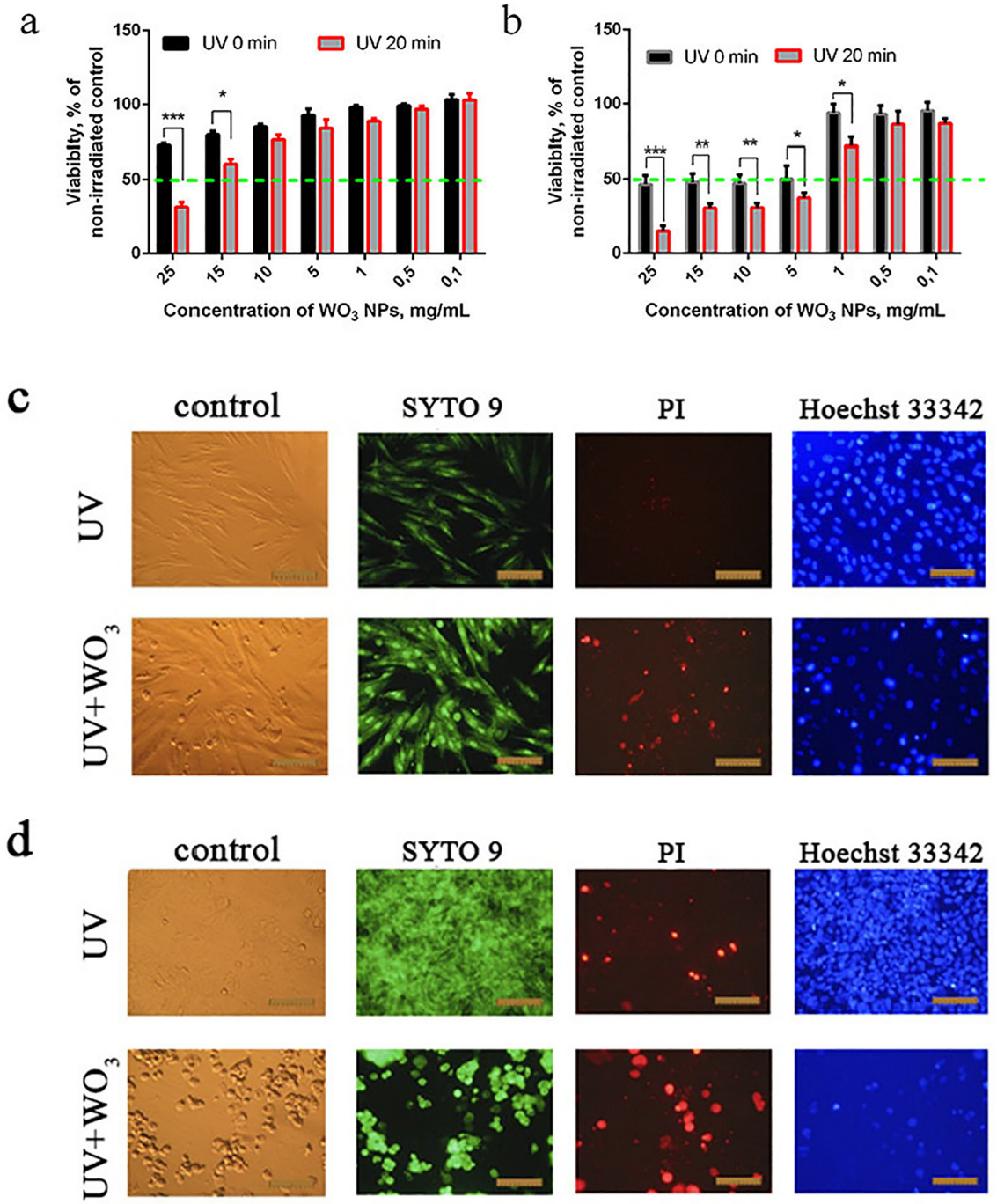

Fig. 12. Analysis of WO_3 NPs' photo-induced cytotoxicity against hMSc and MNNG/Hos cells after 24 h (25 mg/mL WO_3 + 20 min UV irradiation). Morphological features, viability and the number of dead cells were evaluated *via* MTT assay (a, b) and fluorescence microscopy (c, d). Data are expressed as the mean ± SD of three identical experiments (n = 3). Significant difference as compared to the control at *p < 0.01, **p < 0.001, ***p < 0.0001.

normal cells.

It is worth noting the significant activation of the CD34 gene, which is a stemness reduction marker. A significant increase in the level of IL8, which is a marker of cell migration, is also observed for all concentrations of nanoparticles. Moreover, an increase in the concentration of nanoparticles led to a dose-dependent downregulation of proliferation markers (CCNB1, SKP2, CCND1, CCNA2, WEE1, CDC6), confirming the data obtained from the growth curves analysis of cell cultures after incubation with WO_3 NPs (Fig. 6). Thus, after three days of cultivation with WO_3 NPs, cancer cells are at the stage of active death for all WO_3 concentrations tested, which is manifested in a significant suppression of most genes, while normal cells remain viable, due to the activation of antiapoptotic signaling pathways, regulation of redox processes, and cell division. We carried out the analysis of the gene interaction using the web-service https://genemania.org. For the gene interaction analysis, we used all the 96 genes involved in ROS metabolism, apoptosis, necrosis, and autophagy. We showed that the proteins encoded by these genes are involved in the regulation of > 600 different intracellular biological processes (Figs. S5–S7, Tables S1–S4).

It is well known that nanocrystalline tungsten oxide has pronounced photocatalytic activity [14–17]. In this study, we have also evaluated the UV-induced photocytotoxicity of PVP-stabilized WO_3 NPs to normal and cancer cells.

UV irradiation of MNNG/Hos cells incubated with WO_3 NPs lead to

a significant decrease in their viability in a wide range of concentrations (5–25 mg/mL) (Fig. 12b), and also to significant morphological changes in the cells. Meanwhile, hMSc showed a significant decrease in viability only at the highest concentrations of WO_3 NPs (15 and 25 mg/mL) (Fig. 12a). Osteosarcoma cells changed their shape and almost all of them were detached from the substrate after UV irradiation, while hMSc retained their flattened morphology, and only a small number of the cells were detached from the substrate (Fig. 12c, d). One possible reason for this highly selective photocytotoxicity could be the different nature of the cells and their metabolic activity. In particular, it is well known that the metabolism of transformed cells is very specific, especially in terms of oxygen and glucose metabolism. This is true even for cells with fully functioning mitochondria, and is referred to as the Warburg effect. The Warburg effect is an uncommon cause of type B lactic acidosis due to a deregulation of carbohydrate metabolism in neoplastic cells, where lactic fermentation predominates over oxidative phosphorylation, regardless of the oxygenation level [45]. Enhanced glucose metabolism decreases the pH in the microenvironment due to lactate secretion, so the potential benefits of acidosis to cancer cells are multifold [46–48]. We measured the pH of the culture medium after 72 h of cultivation of MNNG/Hos, which was slightly acid (pH 6.7–6.8), while the pH for hMSc was neutral (pH 7.1–7.2). This phenomenon could be the reason for the selective cytotoxic effect of WO_3 NPs on cancer and normal cells.

To estimate the influence of the pH on the photocatalytic activity of PVP-stabilized WO_3 NPs, we irradiated aqueous suspensions of WO_3 NPs having a pH from 4 to 8. For WO_3 NPs, the ability to participate in redox processes is strictly pH-dependent (Figs. S8, S9). Obviously, the oxidative ability of tungsten oxide is more pronounced in the acidic media. It is a well-known fact that W^{+6} ions in tungsten oxide nanoparticles easily undergo reduction, causing the chromism phenomenon and substrate oxidation [20]. This process proceeds faster under illumination, but it can occur in the dark, too; in both cases, the substrate (*e.g.*, cellular components) acts as a reducing agent and undergoes oxidation. WO_3 NPs cause oxidative stress upon uptake due to the generation of reactive oxygen species such as hydrogen peroxide, which results in damage to various biomolecules and changes in the intracellular redox-status. The latter factor leads to the activation of the antioxidant defense system, including overexpression of anti-apoptotic, cell cycle, and pro-inflammatory genes. Different uptake efficiency of WO_3 NPs, as well as different metabolic and redox status in cancer and normal cells, leads to their different response to the presence of WO_3 NPs. It has been reported earlier that the interaction of nanoparticles and living cells begins from their attachment to the cell membrane, due to electrostatic interaction with the subsequent penetration of nanoparticles into the cell [49]. The cells' membranes are negatively charged; PVP-stabilized tungsten oxide nanoparticles have negative ζ-potential in the whole range of pH studied, so the repulsion between nanoparticle and cell should take place. Again, according to Warburg theory, the cancer cells' microenvironment has lowered pH, and the acidic medium leads to a decrease in the absolute ζ-potential value of the particles, which favors their interaction with the membranes.

4. Conclusions

The present study was undertaken to evaluate the cytotoxic effect of PVP-stabilized WO_3 nanoparticles in cancer and normal cell lines. Our results have revealed highly selective WO_3 NPs cytotoxicity to normal and cancer cells. WO_3 NPs have been shown to influence the growth rate of cells, intracellular ROS levels, mitochondrial potential, and expression of genes involved in cellular response to oxidative stress. The highest concentrations of WO_3 NPs (15 and 25 mg/mL) equally inhibited the viability of both types of cells; lower concentrations of WO_3 nanoparticles (1, 5, and 10 mg/mL) were non-toxic to normal cells, which maintained their high viability, while significantly reducing the viability of cancer cells. Selective WO_3 NPs' cytotoxicity is explained by the different rates of proliferation of cell cultures and their inherent metabolic features. It is caused by a high level of anaerobic glycolysis in cancer cells, which results in acidification of the medium and leads to increased levels of intracellular ROS compared to normal cells. Due to their high X-ray attenuating ability and selective anti-cancer activity, WO_3 NPs can be judged to be a promising candidate for the development of new anti-cancer theranostic agents.

Declaration of competing interest

The authors declare no conflict of interest.

Acknowledgments

The work was supported by the Russian Science Foundation (project 18-73-10150).

Appendix A. Supplementary data

Supplementary data to this article can be found online at https://doi.org/10.1016/j.msec.2019.110494.

References

[1] Y. Xia, Nat. Mater. 7 (2008) 758.
[2] J.N. Tiwari, V. Vij, K.C. Kemp, K.S. Kim, ACS Nano 10 (2016) 46.
[3] A.K. Gupta, M. Gupta, Biomaterials 26 (2005) 3995.
[4] X.T. Zheng, A. Ananthanarayanan, K.Q. Luo, P. Chen, Small 11 (2014) 1620.
[5] X. Ren, H. Ma, T. Zhang, Y. Zhang, T. Yan, B. Du, Q. Wei, ACS Appl. Mater. Interfaces 9 (2017) 37637.
[6] X. Ren, J. Yan, D. Wu, Q. Wei, Y. Wan, ACS Sens. 2 (2017) 1267.
[7] L. Yang, D. Fan, Y. Zhang, C. Ding, D. Wu, Q. Wei, H. Ju, Anal. Chem. 91 (2019) 7145.
[8] F. Hosseini, R. Rasuli, V. Jafarian, J. Phys. D. Appl. Phys. 51 (2018) 145403.
[9] M. Firouzi, R. Poursalehi, H.H. Delavari, F. Saba, M.A. Oghabian, Int. J. Biol. Macromol. 98 (2017) 479.
[10] V. Hariharan, S. Radhakrishnan, M. Parthibavarman, R. Dhilipkumar, C. Sekar, Talanta 85 (2011) 2166.
[11] K. Deng, Z. Hou, X. Deng, P. Yang, C. Li, J. Lin, Adv. Funct. Mater. 25 (2015) 7280.
[12] Z. Chen, Q. Wang, H. Wang, L. Zhang, G. Song, L. Song, J. Hu, H. Wang, J. Liu, M. Zhu, D. Zhao, Adv. Mater. 25 (2013) 2095.
[13] S.M. Sharker, S.M. Kim, J.E. Lee, K.H. Choi, G. Shin, S. Lee, K.D. Lee, J.H. Jeong, H. Lee, S.Y. Park, J. Control. Release 217 (2015) 211.
[14] B. Zheng, Y. Bai, H. Chen, H. Pan, W. Ji, X. Gong, X. Wu, H. Wang, J. Chang, Biomater. Sci. 6 (2018) 1379.
[15] J. Liu, J. Han, Z. Kang, R. Golamaully, N. Xu, H. Li, X. Han, Nanoscale 6 (2014) 5770.
[16] A.J. Clark, H.R. Petty, Nanotechnology 27 (2016) 75103.
[17] Z. Zhou, B. Kong, C. Yu, X. Shi, M. Wang, W. Liu, Y. Sun, Y. Zhang, H. Yang, S. Yang, Sci. Rep. 4 (2014) 3653.
[18] L. Wen, L. Chen, S. Zheng, J. Zeng, G. Duan, Y. Wang, G. Wang, Z. Chai, Z. Li, M. Gao, Adv. Mater. 28 (2016) 5072.
[19] W. Guo, C. Guo, N. Zheng, T. Sun, S. Liu, Adv. Mater. 29 (2016) 1604157.
[20] A.L. Popov, N.M. Zholobak, O.I. Balko, O.B. Balko, A.B. Shcherbakov, N.R. Popova, O.S. Ivanova, A.E. Baranchikov, V.K. Ivanov, J. Photochem. Photobiol. B 178 (2018) 395.
[21] T. He, J. Yao, Prog. Mater. Sci. 51 (2006) 810.
[22] X. Jing, D. Zou, Q. Meng, W. Zhang, F. Zhang, W. Feng, X. Han, Inorg. Chem. Commun. 46 (2014) 149.
[23] H.Y. Zhang, L. Xu, E.B. Wang, M. Jiang, A.G. Wu, Z. Li, Mater. Lett. 57 (2003) 1417.
[24] T. Yamase, Chem. Rev. 98 (1998) 307.
[25] N. Oh, J.H. Park, Int. J. Nanomedicine 9 (2014) 51.
[26] V.B. Kumar, C.E. Sawian, D. Mohanta, S. Baruah, N.S. Islam, J. Nanosci. Nanotechnol. 11 (2011) 4659.
[27] Z. Jie, Y. Nosaka, J. Photochem. Photobiol. A 303 (2015) 53.
[28] P. Attri, Y.H. Kim, D.H. Park, J.H. Park, Y.J. Hong, H.S. Uhm, K.N. Kim, A. Fridman, E.H. Choi, Sci. Rep. 5 (2015) 9332.
[29] B. Lipinski, Oxidative Med. Cell. Longev. 2011 (2011) 809696.
[30] L.V. Chekulayeva, I.N. Shevchuk, V.A. Chekulayev, K. Ilmarinen, J. Environ. Pathol. Toxicol. Oncol. 25 (2006) 51.
[31] V. Paget, H. Moche, T. Kortulewski, R. Grall, L. Irbah, F. Nesslany, S. Chevillard, Toxicol. Sci. 143 (2015) 385.
[32] I. Stayton, J. Winiarz, K. Shannon, Y. Ma, Anal. Bioanal. Chem. 394 (2009) 1595.
[33] R. Andrade, L. Crisol, R. Prado, M.D. Boyano, J. Arluzea, J. Aréchaga, Biol. Cell. 102 (2010) 25.
[34] J.D. Ly, D.R. Grubb, A. Lawen, Apoptosis 8 (2003) 115.
[35] S. Fujisawa, Y. Romin, A. Barlas, L.M. Petrovic, M. Turkekul, N. Fan, K. Xu, A.R. Garcia, S. Monette, D.S. Klimstra, J.P. Erinjeri, S.B. Solomon, K. Manova-

Todorova, C.T. Sofocleous, Cytotechnology 66 (2014) 259.
[36] D. Wlodkowic, J. Skommer, C. Hillier, Z. Darzynkiewicz, Cytometry A 73 (2008) 563.
[37] H. Wajant, Science 296 (2002) 1635.
[38] I. Bejarano, J. Espino, D. González-Flores, J.G. Casado, P.C. Redondo, J.A. Rosado, C. Barriga, J.A. Pariente, A.B. Rodríguez, Int. J. Biomed. Sci. 5 (2009) 246.
[39] M. Dizdarogl, P. Jaruga, Free Radic. Res. 46 (2012) 382.
[40] M. Ding, E.R. Kisin, J. Zhao, L. Bowman, Y. Lu, B. Jiang, S. Leonard, V. Vallyathan, V. Castranova, A.R. Murray, B. Fadeel, A.A. Shvedova, Toxicol. Appl. Pharmacol. 241 (2009) 260.
[41] C.V. Dang, Cell 149 (2012) 22.
[42] P.P. Tak, G.S. Firestein, J. Clin. Invest. 107 (2001) 7.
[43] J.T. Opferman, A. Kothari, Cell Death Differ. 25 (2018) 37.
[44] A.M. Yassin, M. Elnouby, N.M. El-Deeb, E.E. Hafez, Appl. Biochem. Biotechnol. 180 (2016) 623.
[45] M.V. Liberti, J.W. Locasale, Trends Biochem. Sci. 41 (2016) 211.
[46] V. Estrella, T. Chen, M. Lloyd, J. Wojtkowiak, H.H. Cornnell, A. Ibrahim-Hashim, K. Bailey, Y. Balagurunathan, J.M. Rothberg, B.F. Sloane, J. Johnson, R.A. Gatenby, R.J. Gillies, Cancer Res. 73 (2013) 1524.
[47] R.A. Gatenby, E.T. Gawlinski, Cancer Res. 56 (1996) 5745.
[48] O.R. Colegio, N.Q. Chu, A.L. Szabo, T. Chu, A.M. Rhebergen, V. Jairam, N. Cyrus, C.E. Brokowski, S.C. Eisenbarth, G.M. Phillips, G.W. Cline, A.J. Phillips, R. Medzhitov, Nature 513 (2014) 559.
[49] F. Mehmood, J. Iqbal, T. Jan, W. Ahmed, W. Ahmed, A. Arshad, Q. Mansoor, S.Z. Ilyas, M. Ismail, I. Ahmad, Ceram. Int. 42 (2016) 14334.